Chem. Res. Chin. Univ., 2016, 32(6), 882—888 doi: 10.1007/s40242-016-6252-x

Tunable Synthesis of Core-shell α-Fe_2O_3/TiO_2 Composite Nanoparticles and Their Visible-light Photocatalytic Activity

SUN Dandan, CAO Yanyan, XU Yanyan*, ZHANG Guoying and SUN Yaqiu

Tianjin Key Laboratory of Structure and Performance for Functional Molecules, Key Laboratory of Inorganic-organic Hybrid Functional Material Chemistry, Ministry of Education, College of Chemistry, Tianjin Normal University, Tianjin 300387, P. R. China

Abstract Uniform α-Fe_2O_3/amorphous TiO_2 core-shell nanocomposites were prepared *via* a hydrolysis method and α-Fe_2O_3/anatase TiO_2 core-shell nanocomposites were obtained *via* a post-calcination process. The structure and morphology of the products were characterized by powder X-ray diffraction, X-ray photoelectron spectroscopy, transmission electron microscopy and scanning electron microscopy. Amorphous TiO_2 nanoparticles with diameters of ten to several tens nanometer were formed on the surface of α-Fe_2O_3 nanoparticles and the coverage density of the secondary TiO_2 nanoparticles in the composite can be controlled by varying the concentration of $Ti(BuO)_4$ in the ethanol solution. The visible-light photocatalytic properties of different products towards Rhodamine B(RhB) were investigated. The results show that the α-Fe_2O_3/amorphous TiO_2 exhibits a good photocatalytic property owing to the extension of the light response range to visible light and the efficient separation of photogenerated electrons and holes between α-Fe_2O_3 and amorphous TiO_2.

Keywords α-Fe_2O_3/TiO_2; Core-shell nanostructure; Photocatalytic activity; Rhodamine B

1 Introduction

Recently, photocatalytic degradation has been recognized as an effective, economic and environment-friendly method to remove toxic organic pollutants from wastewater[1,2]. Metal oxide semiconductor has been widely used as photcatalysts because of their low cost, low toxicity, easy synthesis, and high chemical stability[3—5]. However, owing to the narrow light response range or the low separation efficiency of the photogenerated charge carriers, most of the single-phase semiconductor nanostructures exhibit low efficiency or instability for photocatalytic degradation reaction. Fabricating hybrid semiconductor composites has been proven to be an effective route to improve the photocatalytic activity of photocatalysts[6—11].

As the most stable iron oxide, α-Fe_2O_3 has attracted extensive interest because of its wide commercial and industrial applications in many fields, such as magnetic devices, catalysts, gas sensors, pigments and lithium ion batteries as well as in other biological and medical fields[12—17]. Especially, α-Fe_2O_3 is an n-type semiconductor with a narrow bandgap of 2.1 eV, which is capable of absorbing visible light photons. Thus, α-Fe_2O_3 becomes a promising visible-light-driven photocatalyst[16,18—20]. Unfortunately, comparatively low electronic conductivity of α-Fe_2O_3 results in undesired recombination of photogenerated electron and hole, which restricts its practical application[21]. To settle these problems, an effective method is to couple α-Fe_2O_3 with other semiconductor to form heterostructures/composites. Then, through the transfer of photoinduced electrons and holes between α-Fe_2O_3 and another semiconductor, the charge recombination of photogenerated electrons and holes in the catalyst can be suppressed effectively. Consequently, the catalytic activity of catalysts can be improved greatly. For example, ZnO, TiO_2, SnO_2 and CdS have been proven to be effective counterparts in synthesizing composites with α-Fe_2O_3[22—26]. Among these composites, α-Fe_2O_3/TiO_2 heterostructure is one of the most studied composite due to its high chemical stability, low cost, nontoxicity of TiO_2, and the improved photocatalytic activities of the as-formed composite[20,23,24]. It is reported that the crystallized TiO_2, especially anatase shows relatively high photocatalytic activity[26—28], while amorphous titania with short range ordered structure usually exhibits relatively poor photocatalytic activity because the high density of atomic defects would trap charge carriers and facilitate their recombination[29,30]. However, as an important precursor in the formation of anatase TiO_2, amorphous TiO_2(am-TiO_2) has a much higher surface area which may benefit for adsorbing more substrates and is easy to prepare *via* a mild hydrolytic precipitation route at room

*Corresponding author. E-mail: hxxyxyy@mail.tjnu.edu.cn

Received June 17, 2016; accepted August 4, 2016.

Supported by the National Natural Science Foundation of China(Nos.21001081, 21303122), the High School Science & Technology Fund Planning Project of Tianjin City, China(No.20110510) and the Program for Innovative Research Team in Universities of Tianjin, China(No.TD12-5038).

temperature. In addition, the defect trap sites in amorphous TiO_2 can be worked around by forming a thin shell[31—33]. For example, Lee *et al*.[31] synthesized photocatalysts by coating a thin layer of amorphous TiO_2 on CdSe nanocrystals, which exhibited improved photocatalytic activity for hydrogen evolution from water. Therefore, coating a thin layer of am-TiO_2 on the surface of α-Fe_2O_3 photocatalyst is a simple and effective route to achieve higher photocatalytic activity and stability.

Herein, a simple solution process for the synthesis of uniform α-Fe_2O_3/amorphous TiO_2(α-Fe_2O_3/am-TiO_2) and α-Fe_2O_3/anatase TiO_2(α-Fe_2O_3/an-TiO_2) core-shell nanocomposites was reported. The visible light photocatalytic activity was evaluated by the degradation of RhB in solution and the α-Fe_2O_3/am-TiO_2 composites exhibited better photodegradation activity than neat α-Fe_2O_3 nanoparticles and α-Fe_2O_3/an-TiO_2 core-shell nanocomposite.

2 Experimental

2.1 Synthesis of α-Fe_2O_3/TiO_2 Composite Nanostructures

All the chemicals were of analytical grade and used as received. The α-Fe_2O_3/am-TiO_2 core-shell composites were prepared *via* a two-step solution process. First, the α-Fe_2O_3 nanoparticles were prepared using a surfactant-free solvothermal method previously reported[34] with minor modification. In briefly, 0.055 mol of $FeCl_3 \cdot 6H_2O$ was dissolved into 14.5 mL of deionized water under magnetic stirring to form a yellow and transparent solution, which was then transferred into a Teflon-lined autoclave with a capacity of 20.0 mL and heated at 180 °C for 4 h in an electronic oven. After the completion of the reaction, the autoclave was cooled to room temperature naturally. The red precipitate was collected by centrifugation and washed several times with distilled water and absolute ethanol and dried at ambient temperature. Secondly, 0.02 g of the above obtained α-Fe_2O_3 nanoparticles were dispersed in 30 mL of ethanol under the ultrasonic to form a suspension. Then, an ethanol solution of tetrabutyl titanate[$Ti(BuO)_4$] with a volume ratio of $V_{Ti(BuO)_4}/V_{ethanol}$=0.3 mL/10 mL was dropped into the above suspension under vigorously stirring. After stirring for 2 h, a mixed solution of 0.2 mL of water and 5.0 mL of ethanol was dropped into the above mixture. The mixture was stirred for another 3 h at room temperature, and then the precipitates were separated by centrifugation, washed several times with distilled water and absolute ethanol, dried at ambient temperature. The as-obtained products were the α-Fe_2O_3/am-TiO_2 core-shell composites. To obtain the α-Fe_2O_3/TiO_2 core-shell composites, the α-Fe_2O_3/am-TiO_2 core-shell composites were calcined in a muffle furnace at 450 °C for 2 h under ambient atmosphere.

2.2 Characterization

The phase composition and purity of the products were identified by X-ray diffraction(XRD) on a Bruker D8 ADVANCE diffractometer with Cu $K\alpha$ radiation(λ=0.15418 nm). The morphologies and microstructures of the samples were characterized on a field-emission scanning electron microscope(SEM, FEI NOVA Nano SEM 230), and a high-resolution transmission electron microscope(HRTEM, FEI, Tecnai G2 F20). X-Ray photoelectron spectra(XPS) were recorded on a GENESIS 60S spectrometer to characterize the particles' surfaces with an Al $K\alpha$ line applied as the excitation source. Magnetic measurements were carried out at room temperature on a Quantum Design MPMS SQUID VSM DC magnetometer with the field sweeping from -4×10^6 A/m to 4×10^6 A/m.

2.3 Photocatalytic Evaluation

The photocatalytic activity of the samples was evaluated *via* photocatalytic degradation of Rhodamine B(RhB) under the visible light irradiation(xenon light). The degradation reactions were conducted on an XPA-7 type photochemical reactor (Xujiang Machine Factory, Nanjing, China). The experiment was carried out as follows: 10 mg of the as-prepared samples were dispersed in an RhB solution(2.0×10^{-5} mol/L, 50 mL) and magnetically stirred in the dark for 30 min to reach the adsorption equilibrium. Then, 0.25 mL of a hydrogen peroxide solution(H_2O_2, 30%, mass fraction) was added under magnetic stirring. Then, the solutions were illuminated under a xenon lamp(500 W) with a 420-nm cut off filter at room temperature for 3 h. During the irradiation, the reaction solutions were sampled at 30 min intervals and centrifuged to remove the photocatalyst particles. The dye concentration in the supernatant solution was analyzed by measuring the absorption intensity of RhB at 553 nm.

3 Results and Discussion

Fig.1(A) shows the XRD pattern of the as-obtained products. All the peaks in the XRD pattern can be well indexed to hematite(JCPDS No.33-0664) without the presence of any other diffraction peaks of impurities or TiO_2, indicating that the as-formed TiO_2 from the hydrolysis of $Ti(BuO)_4$ was amorphous. SEM and TEM techniques were used to identify the formation and morphology of the α-Fe_2O_3/am-TiO_2 composites. The SEM image[Fig.1(B)] of the products shows that the sample is consisted of uniform nanoparticles with an average diameter of *ca*. 400 nm, inheriting the morphology and size of core α-Fe_2O_3 nanoparticles well[30]. The surface of the products is consisted of rough and tiny nanoparticles, indicating the formation of the TiO_2 shell layer. Energy dispersive X-ray spectroscopy(EDS) was applied to analyzing the chemical composition of the products[Fig.1(C)]. The peaks associated with Fe, O and Ti elements can be detected in the EDS spectrum, indicating the presence of Ti in the products. The TEM images[Fig.1(D) and (E)] verify that the products are uniform nanoparticles with a thin shell of TiO_2. The HRTEM image of the edge part of a single nanoparticle [Fig.1(F)] clearly shows that a thin amorphous layer is attached to the well-crystallized α-Fe_2O_3 particle. The clear lattice fringe in the inner part of the nanoparticle with interplanar distance of 0.37 nm corresponds to (012) lattice plane of α-Fe_2O_3 crystal.

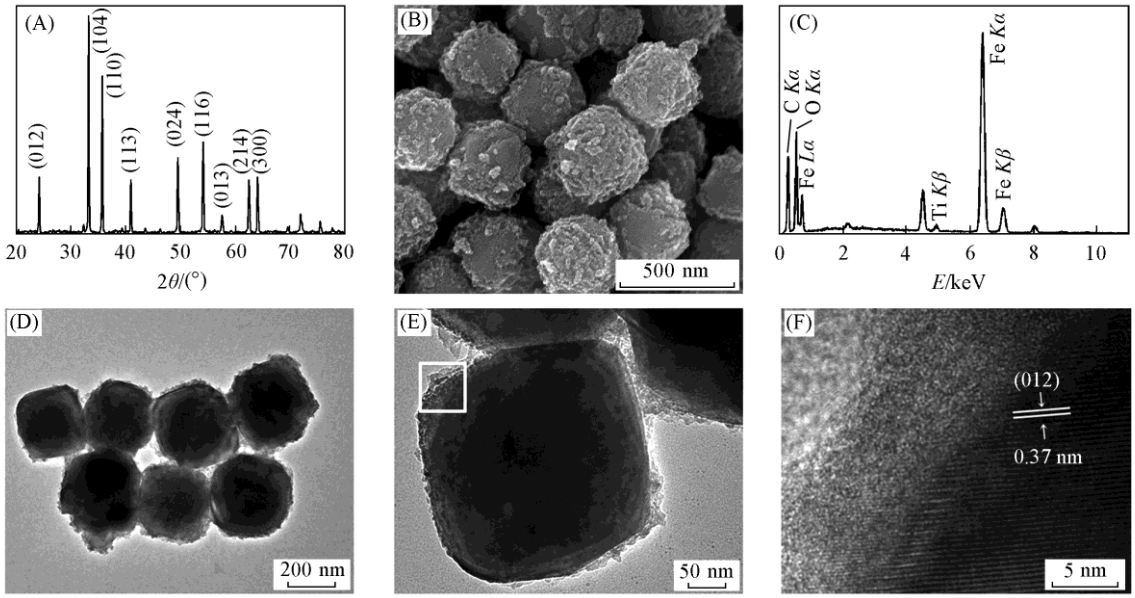

Fig.1 XRD pattern(A), SEM image(B), EDS spectrum(C), lower-magnification TEM image(D), higher-magnification TEM image(E) and HRTEM image(F) of typical α-Fe_2O_3/am-TiO_2 nanostructures

α-Fe_2O_3/an-TiO_2 core-shell composite nanostructures were obtained by calcining the as-prepared α-Fe_2O_3/am-TiO_2 core-shell nanoparticles at 450 °C for 2 h under ambient atmosphere. As shown in Fig.2, both the diffraction peaks of anatase TiO_2(JCPDS No.21-1272) and hematite can be observed, demonstrating the conversion of amorphous TiO_2 to anatase TiO_2 after heat treatment at 450 °C. No other impurity diffraction peaks are discovered, confirming the purity of the products. The SEM images[Fig.2(B) and (C)] show that the products are nanoparticles of *ca*. 400 nm in diameter with uniform size and good dispersity, inheriting the morphology, size and uniformity of the precursor well. From the higher magnification SEM image[Fig.2(C)], it can be seen that the as-formed TiO_2 nanoparticles are of ten to several tens nanometer in diameter and are attached on the surface of the α-Fe_2O_3 nanoparticles. Fig.2(D) and (E) show the typical TEM images of the α-Fe_2O_3/an-TiO_2 core-shell composite nanostructures. From Fig.2(D) and (E), it can be seen that a thin layer of loosely packed nanoparticles covers on the surface of the α-Fe_2O_3 nanoparticle. The HRTEM image of the edge part of the particle marked with the white rectangle is shown in Fig.2(F), which presents two types of lattice fringes. The lattice spacing of the inner part of the particle can be determined to be 0.37 nm, corresponding to the (012) plane of α-Fe_2O_3. The lattice spacing of the edge part of the particle is 0.35 nm, corresponding to the (101) crystallographic plane of anatase TiO_2. The simultaneously presence of α-Fe_2O_3 crystal lattice and TiO_2 crystal lattice in the region of the junction further confirms the formation of α-Fe_2O_3/an-TiO_2 core-shell composite nanostructures.

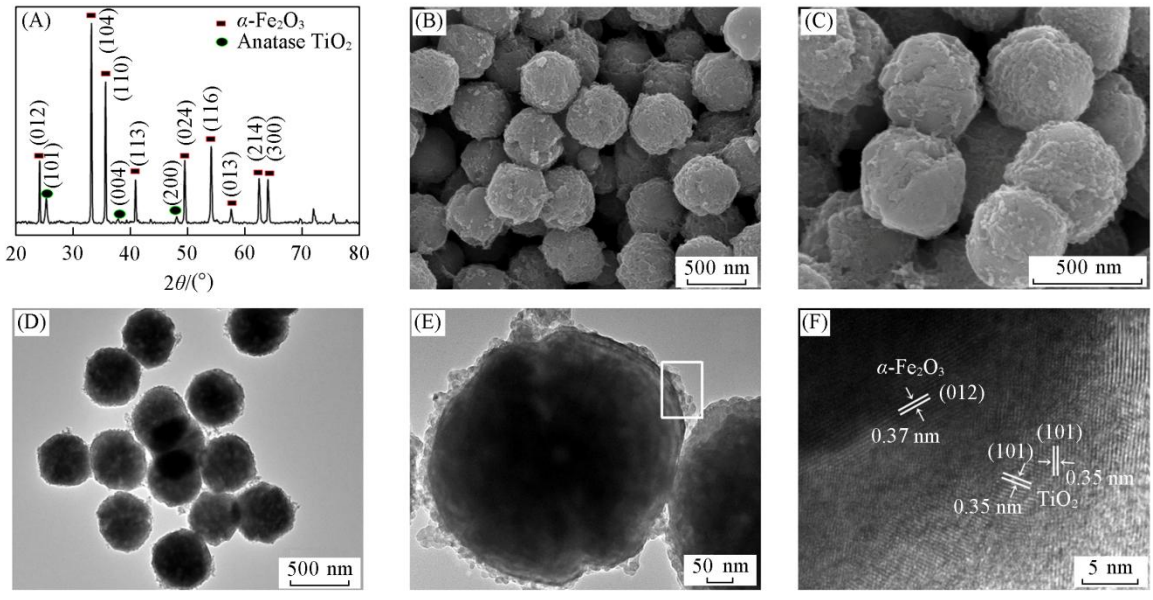

Fig.2 XRD pattern(A), SEM images with lower(B) and higher magnifications(C), TEM images with lower(D) and higher magnifications(E) and HRTEM image(F) of α-Fe_2O_3/an-TiO_2 core-shell composite nanostructures

Based on the analyses of the products in different synthesis stages, the formation mechanism of the core-shell α-Fe_2O_3/TiO_2 composites can be proposed as follows. Core-shell α-Fe_2O_3/am-TiO_2 composites were first obtained after the hydrolysis of $Ti(BuO)_4$ in the solution in the presence of α-Fe_2O_3 particles. Owing to the low concentration of water in the solution, the hydrolysis and condensation rate of $Ti(BuO)_4$ is relatively slow, so that a heterogeneous nucleation of TiO_2 takes place on the surface of α-Fe_2O_3 particles and uniform amorphous TiO_2 shells are formed. Then, when the α-Fe_2O_3/am-TiO_2 core-shell nanostructures were calcined at 450 °C for 2 h under ambient atmosphere, the amorphous TiO_2 was transformed into anatase TiO_2 and the α-Fe_2O_3/an-TiO_2 core-shell composites were formed.

XPS measurement was performed to determine the chemical composition and valence of the calcined sample. The survey XPS spectrum[Fig.3(A)] shows four sets of major peaks which can be assigned to C_{1s}, Ti_{2p}, O_{1s} and Fe_{2p}, respectively. The unexpected C_{1s} peak may be attributed to the adventitious hydrocarbon from the XPS instrument. As shown in Fig.3(B), the peaks located at 711.9 and 725.1 eV can be assigned to $Fe_{2p_{3/2}}$ and $Fe_{2p_{1/2}}$, respectively. A shake-up satellite line at around 719.7 eV represents the Fe^{3+} in Fe_2O_3. Fig.3(C) presents the Ti_{2p} curve of the sample. The two peaks observed at around 458.7 and 464.5 eV can be ascribed to $Ti_{2p_{3/2}}$ and $Ti_{2p_{1/2}}$, respectively. The peak separation between $Ti_{2p_{1/2}}$ and $Ti_{2p_{3/2}}$ levels is 5.8 eV, consistent with the +4 oxidation state of Ti[35].

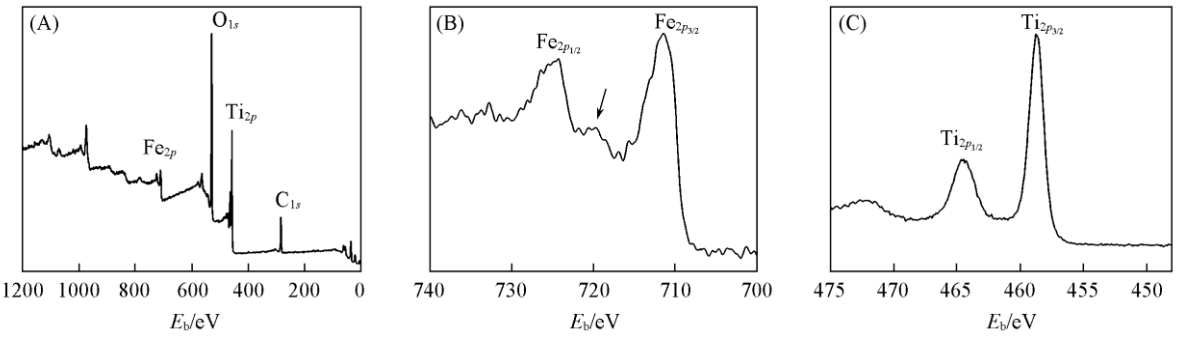

Fig.3 XPS survey spectrum(A), core-level XPS spectra of Fe_{2p}(B), and Ti_{2p}(C) of α-Fe_2O_3/an-TiO_2 core-shell composite nanostructures

The arrow in (B) indicated the Fe^{3+} in Fe_2O_3.

Fig.4 shows the UV-Vis diffuse reflection absorption spectra of the neat TiO_2 prepared using similar hydrolysis and calcination process(which were called amorphous TiO_2 and anatase TiO_2, respectively), the neat α-Fe_2O_3 nanoparticles, α-Fe_2O_3/am-TiO_2 core-shell nanocomposites and α-Fe_2O_3/an-TiO_2 core-shell nanocomposites. Both the amorphous TiO_2 and the calcined anatase TiO_2 particles show clear absorption edges at less than 400 nm and exhibit the intrinsic absorption only in the UV region. In contrast, α-Fe_2O_3/TiO_2 composites show not only strong absorption in the ultraviolet region of less than 400 nm but also a significant enhancement in absorbing the visible light of 400—700 nm compared to that of the pure TiO_2. Meanwhile, compared to that of neat α-Fe_2O_3 nanoparticles, the adsorption intensity of the α-Fe_2O_3/TiO_2 composite enhances obviously.

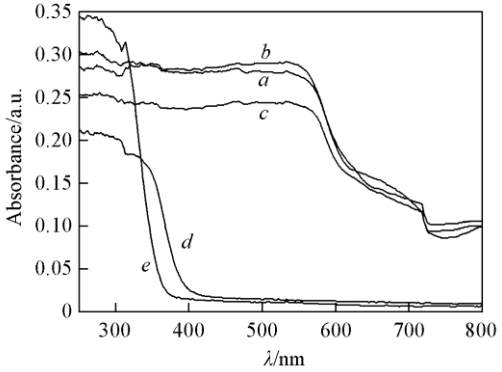

Fig.4 UV-Vis diffuse reflection absorption spectra of α-Fe_2O_3/am-TiO_2 nanocomposites(*a*), α-Fe_2O_3/an-TiO_2 nanocomposites(*b*), α-Fe_2O_3(*c*), anatase TiO_2(*d*) and amorphous TiO_2 particles(*e*)

The magnetic hysteresis measurements of the α-Fe_2O_3/am-TiO_2 nanocomposites and α-Fe_2O_3/an-TiO_2 nanocomposites were carried out at 300 K with the applied magnetic field sweeping from -4×10^6 A/m to 4×10^6 A/m(Fig.5). Similar to that of pure α-Fe_2O_3, the magnetic hysteresis loops of the

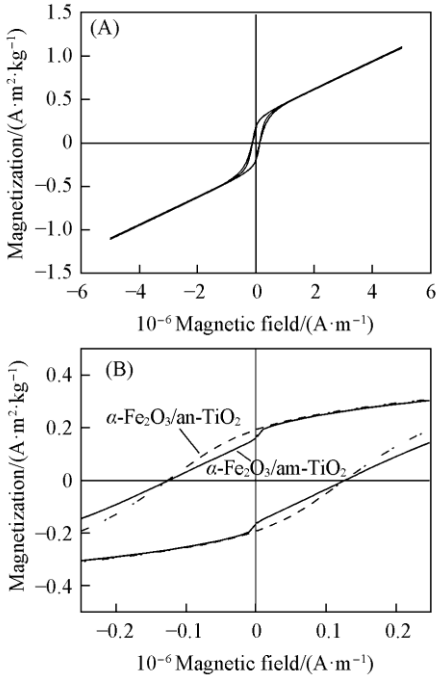

Fig.5 Magnetization curves(A) and corresponding magnified view(B) of α-Fe_2O_3/am-TiO_2 nanocomposite and α-Fe_2O_3/an-TiO_2 nanocomposite measured at 300 K

products show ferromagnetic behavior and no saturation of the magnetization as a function of the field is observed up to the maximum applied magnetic field. As shown in Fig.5(B), the remanent magnetization(M_r) and coercivity force(H_c) are 0.1634 $A\cdot m^2\cdot kg^{-1}$ and 1.01×10^6 A/m for the α-Fe_2O_3/am-TiO_2 nanocomposites, 0.1939 $A\cdot m^2\cdot kg^{-1}$ and 1.01×10^6 A/m for α-Fe_2O_3/an-TiO_2 nanocomposites, respectively. These values were lower than the reported data of the α-Fe_2O_3 truncated octahedral particles, probably because of their smaller size and composited TiO_2 on the surface of α-Fe_2O_3[34,36].

Fig.6 shows the SEM images of the neat α-Fe_2O_3 nanoparticles and α-Fe_2O_3/am-TiO_2 composite nanoparticles prepared with different volume ratios of $Ti(BuO)_4$ to ethanol. As shown in Fig.6(A), the neat α-Fe_2O_3 nanoparticles are quasi-spherical nanoparticles of *ca*. 400 nm in diameter with smooth surface. When the volume ratio of $Ti(BuO)_4$ to ethanol is 1:100(0.1 mL to 10 mL), some TiO_2 nanoparticles are deposited on the surface of the α-Fe_2O_3 nanoparticles[Fig.6(B)]. Then, the amount of the covered TiO_2 nanoparticles increases with the concentration of $Ti(BuO)_4$ in the ethanol solution[Fig.1(B), Fig.6(C) and (D)]. When the volume ratio of $Ti(BuO)_4$ to ethanol is 0.5 mL to 10 mL, the surface of the α-Fe_2O_3 nanoparticles was almost all covered with a thin layer of nanoparticles[Fig.6(D)]. These results suggest that α-Fe_2O_3@TiO_2 composite nanoparticles with different TiO_2 contents are prepared through simple adjusting the concentration of $Ti(BuO)_4$ in the ethanol solution. The corresponding EDS spectra of the sample are shown in Fig.6(E)—(H). The calculated Ti/Fe atom ratios of the four samples prepared with $Ti(BuO)_4$ to ethanol volume ratios of 0.1 mL/10 mL, 0.2 mL/10 mL, 0.3 mL/10 mL, 0.5 mL/10 mL were 1.3%, 8.5%, 12.2%, and 16.0%, respectively, further suggesting that the TiO_2 content in the α-Fe_2O_3/am-TiO_2 composite nanoparticles increases gradually.

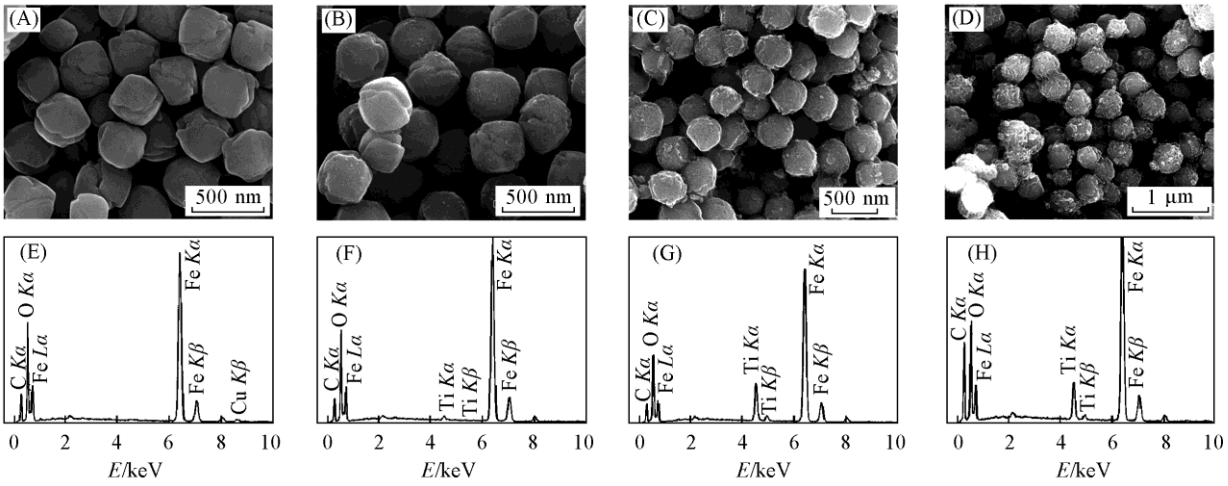

Fig.6 SEM images(A—D) and the corresponding EDS spectra(E—H) of the neat α-Fe_2O_3 nanoparticles(A, E), and α-Fe_2O_3/am-TiO_2 nanocomposites prepared with different volume ratios of $Ti(BuO)_4$ to ethanol

V[$Ti(BuO)_4$]/V(ethanol): (B, F) 0.1 mL/10 mL; (C, G) 0.2 mL/10 mL; (D, H) 0.5 mL/10 mL.

The photocatalytic activity of the typical α-Fe_2O_3/am-TiO_2 composites(as shown in Fig.1) and α-Fe_2O_3/an-TiO_2 composites(Fig.2) was evaluated by photocatalytic degradation of RhB in the presence of H_2O_2 under the visible light illumination. As shown in Fig.7, the real-time degradation curves of RhB as a function of irradiation time display that the concentration decreased to about 98.6% and about 45% of the initial concentration within 150 min for the α-Fe_2O_3/am-TiO_2 nanocomposites and the α-Fe_2O_3/an-TiO_2 nanocomposites, respectively. These results indicate that the photocatalytic property of the α-Fe_2O_3/am-TiO_2 nanocomposites is superior to that of the α-Fe_2O_3/an-TiO_2 nanocomposites. Therefore, the as-prepared α-Fe_2O_3/am-TiO_2 nanocomposites were chosen for further photocatalytic property investigation.

To evaluate the photocatalytic activity of different α-Fe_2O_3/am-TiO_2 nanocomposites, the time-dependent photocatalytic degradation of RhB dye was investigated and compared with that of the P25(TiO_2, Degussa) and neat α-Fe_2O_3 nanoparticles. The different α-Fe_2O_3/am-TiO_2 nanocomposites prepared with volume ratios of $V_{Ti(BuO)_4}/V_{ethanol}$=0.1 mL/10 mL, 0.2 mL/10 mL, 0.3 mL/10 mL and 0.5 mL/10 mL are defined as S**1**, S**2**, S**3**, and S**4**, respectively. As shown in Fig.8(A), both the blank experiment(RhB without any catalyst in the presence of H_2O_2)

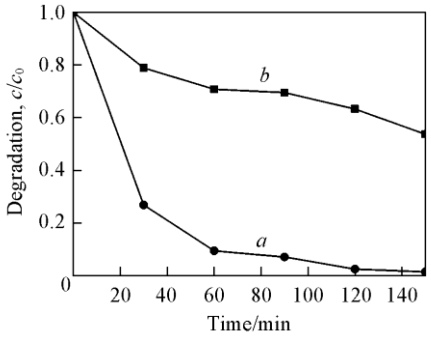

Fig.7 Photocatalytic degradation rate of RhB over the typical α-Fe_2O_3/am-TiO_2 nanocomposites(*a*) and α-Fe_2O_3/an-TiO_2 nanocomposites(*b*) under visible-light illumination in the presence of H_2O_2 additive

c_0 and c are the absorbances from the initial solution and after irradiation, respectively.

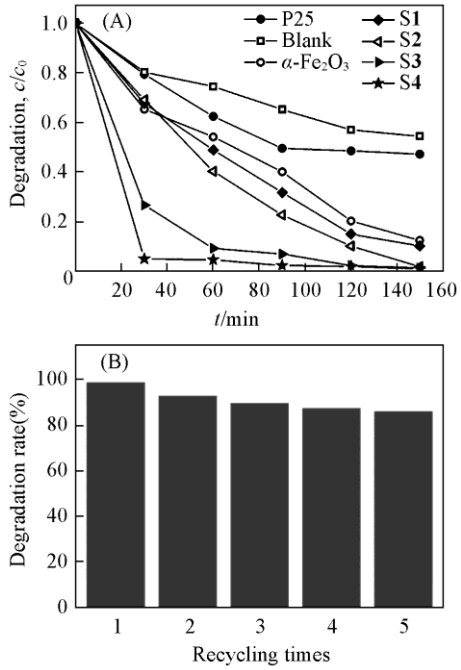

Fig.8 Photocatalytic degradation rate of RhB over different samples under visible-light illumination in the presence of H_2O_2 additive(blank: photolysis of RhB in the presence of H_2O_2 only, P25: TiO_2, Degussa)(A) and the corresponding cycling photodegradation performance of typical α-Fe_2O_3/am-TiO_2 nanocomposites toward 2.0×10^{-5} mol/L RhB solution within five cycles under visible-light irradiation for 150 min(B)

and the controlled experiment using commercial P25 as the catalyst in the presence of H_2O_2 exhibit slow photolysis and only 45.5% and 52.6% of the RhB are degraded after 150 min illumination. While neat α-Fe_2O_3 nanoparticles exhibit higher photocatalytic efficiency compared with that of commercial P25 powder and about 87.4% of the RhB has been degraded after 150 min illumination. Compared with that of the neat α-Fe_2O_3 nanoparticles, the photocatalytic activity of α-Fe_2O_3/am-TiO_2 nanocomposites is increased[Fig.8(A)]. With samples S**1** and S**2** as photocatalysts, the photo-degradation rate of RhB increases slightly, while samples S**3** and S**4** exhibit greatly improved photocatalytic efficiency. For sample S**3**, nearly 98% RhB can be degraded within 120 min. In the presence of sample S**4**, about 95% of the RhB disappears only within 30 min. For samples S**1**, S**2**, S**3** and S**4**, about 89.7%, 98.1%, 98.6% and 98.9% of the RhB can be degraded after 150 min illumination, respectively. These results indicate that the photocatalytic activities of the samples increase with the coverage density of the secondary TiO_2 nanoparticles in the composite. The photocatalytic stability of the α-Fe_2O_3/am-TiO_2 nanocomposites was studied by re-using the recovered catalysts in the next cycle under visible-light irradiation. The typical α-Fe_2O_3/am-TiO_2 composites[as shown in Fig.1 and curve for sample S**3** in Fig.8(A)] were chosen as the catalyst to conduct the photodegradation experiment. Fig.8(B) shows the photodegradation results of RhB for five cycles. It can be seen that the degradation efficiency decreases slightly with prolonged runs, and in the fifth runs about 86% of the RhB has been removed after illuminated by light for 150 min, indicating that the composite photocatalyst is photostable during the photodegradation of RhB.

In the Fenton-like photocatalytic process, the $^{\bullet}OH$ generated from the decomposition of H_2O_2 plays a key role in the degradation of organic dyes. As a narrow bandgap semiconductor, α-Fe_2O_3 can absorb the visible light to generate electron-hole pairs, which can be easily trapped by H_2O_2 to form active hydroxyl radicals($^{\bullet}OH$), as shown in Eqs.(1) and (2). These reactive hydroxyl radicals($^{\bullet}OH$) have high activities and could degrade RhB rapidly. Thus, the efficiency of RhB degradation is promoted upon the addition of α-Fe_2O_3 nanoparticles. However, owing to the fast recombination of the charge carriers generated on the surface of the α-Fe_2O_3 nanoparticles, the efficiency of the neat α-Fe_2O_3 nanoparticles is still limited.

$$\alpha\text{-}Fe_2O_3+h\nu \longrightarrow \alpha\text{-}Fe_2O_3(e^-)+\alpha\text{-}Fe_2O_3(h^+) \quad (1)$$

$$H_2O_2+e^- \longrightarrow OH^-+OH^{\bullet} \quad (2)$$

$$\alpha\text{-}Fe_2O_3(e^-)+ \text{am-}TiO_2 \longrightarrow \text{am-}TiO_2(e^-) \quad (3)$$

For the composite nanostructures, amorphous TiO_2 nanoparticles were formed on the surface of the α-Fe_2O_3 nanoparticles, which would benefit for fast interfacial charge transfer between the two semiconductors. Upon visible light irradiation, the electrons in α-Fe_2O_3 can be excited from valance band(VB) to conduction band(CB). The photo-induced electrons at the CB of α-Fe_2O_3 would be injected into the defect level of amorphous TiO_2, as displayed in Eq.(3), which would promote the separation efficiency of the photogenerated electron-hole pairs and increase the lifetime of the charge carriers[27,37]. Then, the photogenerated electrons have more chance to be captured by H_2O_2 to generate reactive $^{\bullet}OH$ and the photocatalytic efficiency of composite is enhanced largely. Besides the heterostructure characteristic of the composite, the higher photocatalytic activity of the composite also depends on the adsorption of dye on catalyst surface. Coating a thin layer of am-TiO_2 on the surface of the α-Fe_2O_3 nanoparticles may endow the composite larger surface area[38], which would benefit the adsorption of dye on catalyst surface and hence enhance the photocatalytic activity. Therefore, in the composited photocatalysis system, the effective separation of electron-hole pairs and the better adsorption ability of am-TiO_2 for dye molecules are the final reasons for the improvement of the photocatalytic activities.

4 Conclusions

A hydrolysis, crystallization, and post-calcination method was used to prepare uniform α-Fe_2O_3/am-TiO_2 and α-Fe_2O_3/an-TiO_2 core-shell nanocomposites. The TiO_2 nanoparticles with diameter of ten to several tens nanometer was formed on the surface of α-Fe_2O_3 nanoparticles and the coverage density of the secondary TiO_2 nanoparticles in the composite increased the concentration of $Ti(BuO)_4$ in the ethanol solution. The crystalline state of the TiO_2 shell had almost no influence on the magnetic property of the composites, therefore both the

α-Fe_2O_3/am-TiO_2 and α-Fe_2O_3/an-TiO_2 core-shell nanocomposites showed ferromagnetic behavior and similar M_r and H_c value. However, the α-Fe_2O_3/am-TiO_2 composites showed much higher photocatalytic activity toward the degradation of RhB than the α-Fe_2O_3/an-TiO_2 nanocomposites. The photocatalytic activity of the α-Fe_2O_3/am-TiO_2 composites toward the degradation of RhB increased with the TiO_2 contents in the composite. The excellent photocatalytic performance can be attributed to the improved transfer and charge separation of light-induced electrons and holes between α-Fe_2O_3 and amorphous TiO_2.

References

[1] Chen C., Ma W., Zhao J., *Chem. Soc. Rev.*, **2010**, *39*, 4206

[2] Khin M. M., Nair A. S., Babu V. J., Murugan R., Ramakrishna S., *Energy Environ. Sci.*, **2012**, *5*, 8075

[3] Hisatomi T., Kubota J., Domen K., *Chem. Soc. Rev.*, **2014**, *43*, 7520

[4] Schneider J., Matsuoka M., Takeuchi M., Zhang J., Horiuchi Y., Anpo M., Bahnemann D. W., *Chem. Rev.*, **2014**, *114*, 9919

[5] Mishra M., Chun D. M., *Appl. Catal. A: Gen.*, **2015**, *498*,126

[6] Rajeshwar K., Tacconi N. R., Chenthamarakshan C. R., *Chem. Mater.*, **2001**, *13*, 2765

[7] Dong S., Feng J., Fan M., Pi Y., Hu L., Han X., Liu M., Sun J., Sun J., *RSC Adv.*, **2015**, *5*, 14610

[8] Wu W., Jiang C., Roy V.A.L., *Nano Scale*, **2015**, *7*, 38

[9] Wang H., Liu N., Lu J., Yao S., Jiang S., Zhang W., *Chem. Res. Chinese Universities*, **2015**, *31*(5), 846

[10] Ma J., Wang K., Li L., Zhang T., Kong Y., Komarneni S., *Ceram. Int.*, **2015**, *41*, 2050

[11] Xu Z., Huang C., Wang L., Pan X., Qin L., Guo X., Zhang G., *Ind. Eng. Chem. Res.*, **2015**, *54*, 4593

[12] Wheeler D. A., Wang G., Ling Y., Li Y., Zhang J. Z., *Energy Environ. Sci.*, **2012**, *5*, 6682

[13] Jain G., Balasubramanian M., Xu J., *Chem. Mater.*, **2006**, *18*, 423

[14] Chen J., Xu L. N., Li W. Y., Gou X. L., *Adv. Mater.*, **2005**, *17*, 582

[15] Zhou X., Lan J., Liu G., Deng K., Yang Y., Nie G., Yu J., Zhi L., *Angew. Chem. Int. Ed.*, **2012**, *51*, 178

[16] Jagadeesan D., Mansoori U., Mandal P., Sundaresan A., Eswaramoorthy M., *Angew. Chem. Int. Ed*., **2008**, *47*, 7685

[17] Liu X., Liu J., Chang Z., Luo L., Lei X., Sun X., *RSC Adv.*, **2013**, *3*, 8489

[18] Yu J., Yu X., Huang B., Zhang X., Dai Y., *Cryst. Growth Des.*, **2009**, *9*, 1474

[19] Zhou X., Yang H., Wang C., Mao X., Wang Y., Yang Y., Liu G., *J. Phys. Chem. C*, **2010**, *114*, 17051

[20] Liu G., Deng Q., Wang H., Ng D. H. L., Kong M., Cai W., Wang G., *J. Mater. Chem.*, **2012**, *22*, 9704

[21] Zhu S., Yao F., Yin C., Li Y., Peng W., Ma J., Zhang D., *Microporous Mesoporous Mater.*, **2014**, *190*, 10

[22] Wu W., Zhang S., Xiao X., Zhou J., Ren F., Sun L., Jiang C., *ACS Appl. Mater. Interfaces*, **2012**, *4*, 3602

[23] Liu J., Yang S., Wu W., Tian Q., Cui S., Dai Z., Ren F., Xiao X., Jiang C., *ACS Sustainable Chem. Eng.*, **2015**, *3*, 2975

[24] Wu W., Zhang S., Ren F., Xiao X., Zhou J., Jiang C., *Nanoscale*, **2011**, *3*, 4676

[25] Shi Y., Li H., Wang L., Shen W., Chen H., *ACS Appl. Mater. Interfaces*, **2012**, *4*, 4800

[26] Pan J., Li X., Zhao Q., Zhang D., *RSC Adv.*, **2015**, *5*, 51308

[27] Wang X., Yang W., Li F., Zhao J., Liu R., Liu S., Li B., *J. Hazard. Mater.*, **2015**, *292*, 126

[28] Li W. B., Feng C., Yue J. G., Hua F. X., Bu Y. Y., *Chem. J. Chinese Universities*, **2015**, *36*(6), 1194

[29] Ohtani B., Ogawa Y., Nishimoto S., *J. Phys. Chem. B*, **1997**, *101*, 3746

[30] Wang Q., Chen M., Zhu N., Shi X., Jin H., Zhang Y., Cong Y., *J. Colloid Interface Sci.*, **2015**, *448*, 407

[31] Lee S., Lee K., Kim W. D., Lee S., Shin D. J., Lee D. C., *J. Phys. Chem. C*, **2014**, *118*, 23627

[32] Wang C. J., Kwon K. W., Odlyzko M. L., Lee B. H., Shim M., *J. Phys. Chem. C*, **2007**, *111*, 11734

[33] Tian X., Li S., Cao Y., Xu Y., Zhang G., *Mater. Lett.*, **2014**, *131*, 86

[34] Yang S., Xu Y., Sun Y., Zhang G., Gao D., *Cryst. Eng. Comm.*, **2012**, *14*, 7915

[35] Amarjargal A., Jiang Z., Tijing L. D., Park C. H., Im I. T., Kim C. S., *J. Alloys Compd.*, **2013**, *580*, 143

[36] Wu W., Zhang S., Xiao X., Zhou J., Ren F., Sun L., Jiang C., *ACS Appl. Mater. Interface*s, **2012**, *4*, 3602

[37] Zang L., Lange C., Abraham I., Storck S., Maier W. F., Kisch H., *J. Phys. Chem. B*, **1998**, *102*, 10765

[38] Wei X. X., Cui H. T., Guo S. Q., Zhao L. F., Li W., *J. Hazard. Mater.*, **2013**, *263*, 650